Experimental assessment of woody biomass gasification in a hybridized solar powered reactor featuring direct and indirect heating modes

Axel Curcio [a], Sylvain Rodat [a], Valéry Vuillerme [b], Stéphane Abanades [a,*]

[a] *Processes, Materials and Solar Energy Laboratory, PROMES - CNRS, 7 Rue Du Four Solaire, 66120, Font-Romeu Odeillo, France*
[b] *Univ. Grenoble Alpes INES - CEA, 50 Avenue Lac Léman, 73375, Le Bourget-du-Lac, France*

HIGHLIGHTS

- A 1.5 kW_{th} spouted bed solar gasifier was studied under both direct and indirect heating.
- Impact of hybrid allothermal-autothermal operation on syngas production was investigated.
- $H_2O–O_2$ gasification was assessed at thermodynamic equilibrium and validated experimentally.
- High temperatures (~1300 °C) and direct heating favored both allothermal and hybrid operation.
- A 40% cut of the solar power input was counterbalanced by addition of biomass and oxygen.

GRAPHICAL ABSTRACT
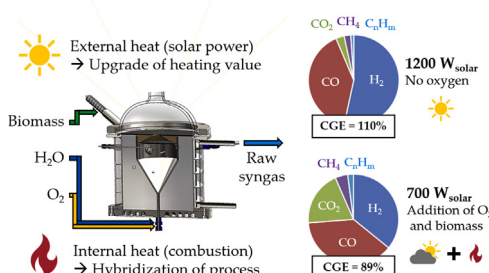
ABSTRACT

Solar thermochemical gasification is an opportunity for the production of sustainable fuels from carbonaceous resources including biomass. Substituting conventional gasification processes by solar-driven technologies may enable cleaner production of H_2-rich syngas while saving feedstock resources and alleviating CO_2 emissions. This work addresses hybrid solar-autothermal gasification of mm-sized beech wood particles in a lab-scale 1.5 kW_{th} spouted-bed reactor. Hybridization under reduced solar power input was performed by injecting oxygen and additional biomass inside the gasifier for complementary heat supply. Increasing O_2:C molar ratios (in the range 0.14–0.58) allowed to heat the reactor cavity and walls progressively, while gradually impairing the reactor performance with an increase of the syngas CO_2 content and a decrease of the reactor cold gas efficiency (CGE). Gasification with mixed H_2O and O_2 was then assessed at thermodynamic equilibrium and global trends were validated experimentally, showing that control of H_2:CO ratio was compatible with in-situ combustion. The impact of reaction temperature (1200–1300 °C)

---

* Corresponding author.
  E-mail address: stephane.abanades@promes.cnrs.fr (S. Abanades).
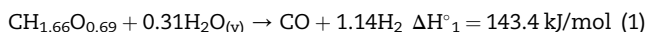
Concentrated solar energy
Continuous operation

and heating mode (direct or indirect) was experimentally studied during both allothermal and hybrid gasification. Higher H_2 and CO yields were achieved at high temperatures (1300 °C) under direct reactor heating. Hybridization was able to counterbalance a 40% drop of the nominal solar power input, and the measured CGE reached 0.82, versus values higher than 1 during allothermal gasification.
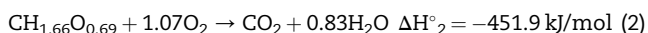
Introduction

Solar gasification of biomass into a hydrogen-rich syngas has been developed for both power generation and chemical process integration. Since the first solar gasification experiments in 1980 [1], high storage potential of solar energy has been reported and solar gasification process economics has been assessed [2,3]. Different solar reactor designs were proposed [3–5] including packed bed gasifiers [6–9], fluidized beds [6,10], vortex-flow reactors [11], and molten-salt and molten-slag based designs [12,13]. More recently, dual fluidized-bed reactors [14–17], vortex-flow [18,19], spouted-bed [20–22], and molten-salt based gasifiers [23,24] have been considered. However, in order to overcome the variability of solar resource, reactor hybridization has been recently investigated to ensure both allothermal (solar only) and hybrid allothermal-autothermal (combustion-aided) gasification. Boujjat et al. [25] experimentally studied beech wood gasification by steam at temperatures in the range 1200–1300 °C (Equation (1)). Injection of oxygen and additional biomass aimed to initiate combustion (Equation (2)), in order to compensate for solar power input daily variations. Partial oxidation might also take place to a certain extent (Equation (3)), leading to a less endothermic production of H_2 and CO.
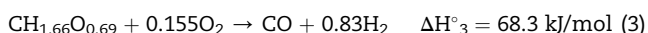
Steam gasification of dry beech wood:

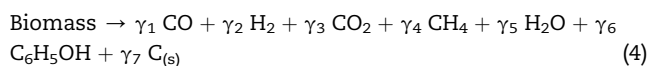$$CH_{1.66}O_{0.69} + 0.31H_2O_{(v)} \rightarrow CO + 1.14H_2 \quad \Delta H°_1 = 143.4 \text{ kJ/mol} \quad (1)$$

Oxy-combustion of dry beech wood:

$$CH_{1.66}O_{0.69} + 1.07O_2 \rightarrow CO_2 + 0.83H_2O \quad \Delta H°_2 = -451.9 \text{ kJ/mol} \quad (2)$$

Partial oxidation of dry beech wood:

$$CH_{1.66}O_{0.69} + 0.155O_2 \rightarrow CO + 0.83H_2 \quad \Delta H°_3 = 68.3 \text{ kJ/mol} \quad (3)$$
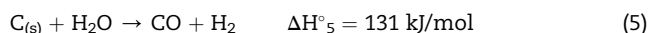
The actual gasification mechanism comprises multiple side reactions. The two major ones are the pyrolysis of the carbonaceous feedstock (thermal devolatilization of biomass into char, steam, light gases and tars) and the gasification of char (highly endothermic oxidation into H_2 and CO). The distribution of pyrolysis products varies a lot from one experimental setup to another, depending on the heating rate, residence time and biomass characteristics, and so does the reaction enthalpy. The general reaction used by Boujjat et al. [26] in their modelling work is given in Equation (4), where phenol accounts for intermediate tars and hydrocarbons. Char gasification (Equation (5)) has been well mastered since

the 1930s [27], and it is known for working in pair with the water-gas shift reaction [28] that regulates the balance between H_2 and CO quantities (Equation (6)). Hydrogen and carbon monoxide are also produced via steam reforming reaction (Equation (7)). Numerous other reaction mechanisms have been detailed to account for the formation of gas hydrocarbons and tars [29]. Modelling techniques such as distributed activation energy model and multi-box approach have been confronted [30,31], but no universal model is yet used for all gasifier designs, as the reaction is strongly dependent on operating conditions (feedstock characteristics, reaction temperature, and pressure).
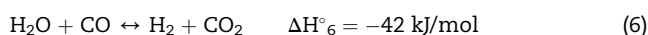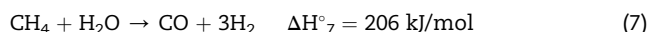
Pyrolysis of biomass:

$$\text{Biomass} \rightarrow \gamma_1 \text{ CO} + \gamma_2 \text{ H}_2 + \gamma_3 \text{ CO}_2 + \gamma_4 \text{ CH}_4 + \gamma_5 \text{ H}_2\text{O} + \gamma_6 \text{ C}_6\text{H}_5\text{OH} + \gamma_7 \text{ C}_{(s)} \quad (4)$$

Gasification of char:

$$C_{(s)} + H_2O \rightarrow CO + H_2 \quad \Delta H°_5 = 131 \text{ kJ/mol} \quad (5)$$

Water-gas shift:

$$H_2O + CO \leftrightarrow H_2 + CO_2 \quad \Delta H°_6 = -42 \text{ kJ/mol} \quad (6)$$

Steam methane reforming:

$$CH_4 + H_2O \rightarrow CO + 3H_2 \quad \Delta H°_7 = 206 \text{ kJ/mol} \quad (7)$$

In the domain of spouted-bed technologies, recent research works tackled the impact of temperature (in the range 800–900 °C) on tars formation [32], or the impact of gases flow rates, biomass properties and temperature (in the range 1100–1300 °C) on gasifier performance [33,34]. Addition of a bed of inert particles (alumina, SiC, olivine, sand) has also been investigated to improve the thermal inertia of solar reactors [35]. Besides, the effect of simultaneous steam and oxygen injection has been mapped during fully autothermal [36] and hybrid [37] operation. In the latter case, optimal reactant flow rates were identified as a function of the solar flux by thermodynamic calculations. Regarding advanced control strategies, Petrasch et al. [38] introduced a simplified feedback method that was applied to existing solar allothermal gasifier designs. The CO_2 concentration in the syngas was controlled by modifying the steam input flow rate, which resulted in improved reactor efficiency over time. Saade et al. [39] applied a model predictive control algorithm to manage the output $CO:CO_2$ ratio using a highly non-linear model of the reactor. Then, in the field of combustion-aided gasification,

Muroyama et al. [40] used a linear dynamic model to control the temperature of a fluidized-bed reactor through simultaneous injection of O_2 and additional feedstock. This resulted in a reduction of the theoretical CO_2 emission in the range 17.8–22.8% between fully autothermal mode and hybrid operation depending on the season. Boujjat et al. [41] proposed an extrapolated 0D model based on thermodynamic equilibrium to validate the feasibility of dynamic control over the year. They assessed the impact of hybridization on syngas quality: in particular, the H_2:CO mole ratio dropped from 1.2 to 0.8 between solar-only and hybrid regimes. Experiments carried out by Muroyama et al. [42] demonstrated that this effect could be countered by injecting additional steam in hybrid mode. In general, tuning of the syngas quality might be possible by adjusting both steam and oxygen injection, which was detailed by Li et al. [37] on the basis of thermodynamic analysis. Hathaway et al. [43] recently adapted their molten-salt-based gasifier to perform hybrid operation and to control the H_2:CO ratio, with an experimental validation that steam addition could permit to control the syngas quality (via steam shifting). This objective was justified by the need to integrate solar hybrid gasifiers into continuous industrial demonstrators and to provide a constant syngas output composition for stable downstream processing. To date, limited experimental work was carried out in this field and data are required to bridge the gap between theoretical results with practical observations. In addition, insights into the process dynamic behavior are of special interest.

This study presents experimental results obtained in a hybridized spouted-bed solar gasifier. The goal is to validate the feasibility of continuous wood gasification under decreasing solar power input, thanks to hybrid solar-autothermal operation. A study of the impact of oxygen to carbon ratio (O_2:C) in the feed and of the combination of oxygen with steam is provided, to identify precise trends regarding reactor performance and to compare them to calculations made at thermodynamic equilibrium (TE). The role of temperature is assessed in the range 1200–1300 °C during both allothermal and hybrid gasification, and the performances achieved under direct and indirect heating modes are compared during continuous hybrid operation. Finally, the dynamics of hybridization during a decrease of the solar power input are discussed.

Materials and methods

The lab-scale gasifier, detailed in Fig. 1, was operated under real concentrated solar power. Incident sunlight was reflected upwards by a heliostat and was concentrated by a parabolic mirror of 2 m diameter placed above the reactor. After crossing the glass window positioned at the top of the reactor, the concentrated solar flux entered the cavity via a small aperture (20 mm diameter) on the alumina cap. This front aperture plate was covered with a layer of zirconia and graphite felts to reduce radiation losses. The power absorbed by the reactor cavity under a DNI (Direct Normal Irradiation) of 1 kW/m^2 equaled ~1.5 kW$_{th}$, according to calorimetry measurements. In direct heating mode, concentrated sunlight directly entered the cavity. In indirect heating mode, an

additional 2 mm-thick SiC-coated graphite plate was set below the alumina cap to absorb solar radiation and re-emit heat as infrared radiation towards the bottom cavity. The reactor cavity was insulated by a surrounding 3 cm thick layer of porous ceramic fiber. A water circuit allowed cooling of the external stainless-steel reactor envelope.

Spouting of the particles was achieved in a 68 mm high and 60° cone topped by a cylindrical piece (78 mm inner diameter), both made of a high-temperature resistant metallic FeCrAl alloy. The cavity volume (comprised under the position of the emitter plate) was 0.24 L. Irregularly-shaped beech wood particles (Fig. 1, characteristics given in Table 1) were fed by a screw driver in the upper part of the cavity and dropped by gravity inside the cavity. Oxidizing agents mixed with a flow of argon (0.2 NL/min) were provided down the cavity with sufficient velocity to vigorously stir the bulk reacting solid. Argon was also injected through the hopper and screw driver (0.5 NL/min) with the biomass to limit counterflow heat and mass transfer in the injection tube, and in the window region (2 NL/min) to keep it clean from pyrolytic gases. A 1.5 cm-height bed of Al_2O_3 inert particles (2–3 mm size) was placed at the cone base to protect the injection tube from thin char and ash residues.

Inlet gas flow rates were managed by mass flow controllers (BROOKS 5850 S). Water injection was ensured by a liquid mass flow controller (HORIBA SILV-F30P). Wood particles were injected by a screw driver calibrated before the experimental campaign. Outlet syngas concentrations (H_2, CO, CO_2, CH_4) were measured by an online analyzer (GEIT GAS 3100 SYN-GAS, one measurement every 3 s) and by a gas chromatograph (GC, Varian CP49000, one measurement every 2 or 3 min) after the outlet gas flowed through a bubbler and two micro-filters to remove remaining moisture and entrained char particles. GC was mainly used to measure yields of light gas hydrocarbons (C_2H_m, as the sum of C_2H_2, C_2H_4 and C_2H_6 species, precision of ±1%).

Located at the center of the parabolic mirror, a solar-blind pyrometer (4.8–5.2 μm, pointing through a CaF_2 window) estimated the temperature (T_{pyro}) of the emitter plate (in indirect heating mode) or the temperature of the bulk solid inside the spouted-bed (in direct heating mode). The temperature of the conical cavity external wall, which was found to be quite homogeneous [44], was measured by a B-type thermocouple (T_2). Another thermocouple, shielded with an alumina tube, was placed inside the cavity to estimate the temperature at its center (T_3). Pressures were also monitored, though they usually stayed slightly above atmospheric pressure (0.85–0.90 atm due to the location of the laboratory at an altitude of 1600 m).

Syngas compositions were systematically compared with compositions calculated at Thermodynamic Equilibrium (TE), by minimizing the system's Gibbs free energy under similar operating conditions (closed system approach). This was done using the CANTERA [45] open library in Python, which featured a calculation environment with a rich database of species thermodynamic properties. Char was modeled by solid graphite, and species taken from the GRI30 dataset were used to model the gas phase. The input biomass and oxidant were represented by an equivalent mixture of char, H_2 and O_2. TE was calculated under constant temperature and pressure
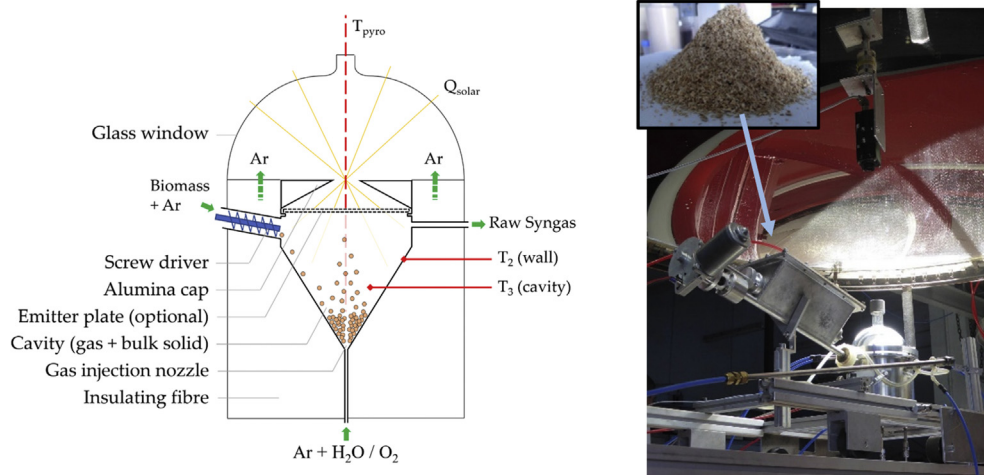
Fig. 1 – Scheme and photograph of the solar gasification reactor (inset: photograph of the beech wood particles).

Table 1 – Beech wood characteristics (dry basis).

C (wt.%)	H (wt.%)	O (wt.%)	N (wt.%)	S (wt.%)	Ash (wt.%)	Cl (wt.%)	Moisture (wt.%)	LHV (MJ/kg)	Diameter
48.3	6.7	44.4	0.1	<0.1%	0.4	<0.1%	8.9	16.8	<2 mm

conditions (always set to 0.85 atm). Only the species with mole fractions greater than 1×10^{-3} were discussed, including generally H_2, CO, CO_2, H_2O and char, as neither CH_4 nor heavier gases were found at temperatures higher than 1200 °C.

Results and discussion

In total, 12 solar runs were conducted (Table 2). Except for runs #3 and #4, they were all planned in pairs (same operating conditions for both direct and indirect heating modes). The set

points for wood (1.2–1.4 g/min), steam (0–0.25 g/min) and oxygen (0–0.38 NL/min) flow rates are given in Table 2. They were often changed during operation in order to observe dynamic impacts on the evolution of syngas production. At the beginning of all runs, the temperature measured in the cavity was stabilized at a nominal value (initial T_3 temperature) by adjusting the solar power supply (via partial closure of the trapdoor shutter below the reactor). Gasification was then performed under a fixed solar power input, except for runs #11 and #12 that featured a partial trapdoor closure (for cutting the sunlight source by 40%) to simulate a decrease of the solar power input (e.g., simulation of passing clouds).

Table 2 – Operating conditions and overall reactor performance for the solar gasification runs.

Run #	Heating mode	Initial T_3 temperature [°C]	Wood flow rate [g/min]	Steam flow rate [g/min]	Oxygen flow rate [NL/min]	CCE	CGE	SFE
1	Direct	1215	1.2	0	0.1–0.25–0.38	81.6%	65.0%	–
2	Indirect	1190	1.2	0	0.25–0.38–0.1–0.25–0.38	78.7%	60.1%	–
3	Indirect	1265	1.2	0	0	35.4%	46.8%	–
4	Indirect	1205	1.2	0	0.25	80.7%	72.4%	–
			1.4	0.2				
5	Direct	1200	1.2	0.2	0	82.9%	78.6%	17.1%
			1.4		0.25			
6	Indirect	1180	1.2	0.2	0	82.0%	77.3%	18.7%
			1.4		0.25			
7	Direct	1315	1.2	0.2	0	83.6%	97.4%	20.6%
			1.4		0.25			
8	Indirect	1305	1.2	0.2	0	81.4%	86.1%	18.9%
			1.4		0.25			
9	Direct	1215	1.4	0.2	0.25	83.7%	82.4%	23.6%
10	Indirect	1215	1.4	0.2	0.25	86.2%	81.6%	15.6%
11	Direct	1335	1.2	0.2	0	86.8%	99.8%	27.4%
			1.4		0.25			
12	Indirect	1325	1.2	0.2	0	88.3%	100.0%	28.3%
			1.4		0.25			

Carbon conversion efficiencies and cold gas efficiencies are given in Table 2. These values were calculated over the entire duration of runs, which includes all transient regimes and interruption periods. They thus provide a performance indication for the whole solar experiments. The carbon conversion efficiency (CCE) corresponds to the fraction of carbon atoms injected in the form of biomass that ends in the syngas in the form of CO, CO_2, CH_4 and gas hydrocarbons (mainly C_2H_2 and C_2H_4). CCE inferior to unity is explained by char remaining unconverted, and by thin char particles entrained by the gas flow and filtered. The former carbon conversion loss reflects the incompleteness of the gasification reaction, while the latter one is due to the gasifier design that leads some particles to escape the cavity before their full conversion. The cold gas efficiency (CGE) is the ratio between syngas and biomass LHV (lower heating value, MJ/kg) multiplied by their respective masses. It measures how well the biomass is converted into syngas and quantifies the improvement (if higher than 1) of the calorific value between the initial feedstock and the produced fuel. Finally, the solar-to-fuel energy conversion efficiency was calculated, as defined in Equation (8) [25]. Unlike CGE, it includes at denominator the total solar energy absorbed by the gasifier during the biomass injection periods. Its values ranged between 16% and 28%.

$$SFE = \frac{LHV_{syngas} \cdot m_{syngas}}{Q_{solar} + LHV_{feedstock} \cdot m_{feedstock}} \qquad (8)$$

First of all, experimental results focused on the impact of oxygen flow rate on syngas quality (runs #1 and #2). Results obtained with different combinations of H_2O and O_2 were also compared (runs #3 and #4). Then, the transition from allothermal to hybrid solar-autothermal operation was studied under constant solar power input (runs #5 to #8 at several operating temperatures), and continuous hybrid gasification was carried out to assess the differences between direct and indirect heating modes (runs #9 and #10). Finally, two allothermal-hybrid runs under both direct and indirect heating were performed while simulating a drop of solar power input (runs #11 and #12). A summary of the experimental results is given in Supplementary Material (Table S1).

Impact of oxygen injection flow rate

In runs #1 and #2, syngas was produced under several O_2 flow rates (0.1, 0.25, and 0.38 NL/min). Experiments were carried out under a very stable DNI (maximum variation of 1.7%) at ~1200 °C, with a mean solar power input of 0.76 kW$_{th}$. Three and five wood-oxygen injections were performed in direct and indirect heating modes respectively. Between injections, 3 to 5-min interruptions of the screw driver were set to ensure consumption of the accumulated char by the continuous oxygen stream. Fig. 2 shows the output volume flow rates of the main syngas components, measured during the three first injection periods of run #2. The entire evolution curves for runs #1 and #2 are provided in Fig. S1 and Fig. S2, respectively. In all cases, the output flow rate of O_2 reached zero during biomass injection periods (while both H_2 and CO are produced). In contrast, when wood injection was stopped, the slowly decreasing CO_2 and slowly increasing O_2 flow rates

indicated that some remaining char was burnt. Sharper changes of the output O_2 flow rates (increase at 10 min and decrease at 19 min, Fig. 2) were due to the change of the input flow rate. Besides, the more O_2 was injected, the more CO_2 was produced (up to 0.3 NL/min at the highest O_2 injection rate). The production rate of CH_4 rather tended to decrease with increasing O_2 flow rate. The total yields of produced species were calculated for thorough comparison between all injection periods, and plotted in Fig. 3.

To calculate the gas production yields (per unit mass of dry feedstock), the mass of wood provided during each injection was corrected pro rata the distribution of output gas masses. Indeed, the wood injection rate tended to decrease over time even though the screw driver was operated at a constant rate. This occurred progressively while the hopper was emptying, which caused the actual inlet O_2:C ratios to become progressively greater than the expected values. The actual O_2:C ratios were thus calculated a posteriori: a mass balance was performed for each injection period to determine the specific gas yields (Fig. 3) and reactor efficiencies (Fig. 4-b). It appeared that the CO_2 yield increased proportionally to the O_2:C ratio, reaching up to 18.5 mmol/g$_{wood,dry}$ at a ratio of 0.58 (indirect heating). On the contrary, the quantities of H_2, CO, CH_4 and C_2H_m decreased when the O_2 injection rate increased. For instance, in direct heating mode, the H_2 and CO yields ranged from 20 to 10 mmol/g$_{wood,dry}$ (H_2) and from 21 to 17 mmol/g$_{wood,dry}$ (CO) for O_2:C ranging from 0.14 to 0.47.

The mole fractions of H_2, CO, and CO_2 (dried syngas) are plotted in Fig. 4-a as a function of the O_2:C ratio, and they are compared to the fractions calculated at TE at 1200 °C. Calculations show that at equilibrium, when the oxidant quantity is high enough to gasify all the char (O_2:C > 0.09), CO_2 is produced in growing quantities while both H_2 and CO fractions decrease simultaneously. The measured H_2 and CO mole fractions followed the decreasing trends predicted by TE, with CO fractions remaining steady for O_2:C values between 0.18 and 0.33 (as seen in Fig. 3 in indirect heating mode). The H_2 and CO mole fraction measurements were lower than values computed at TE, whereas CO_2 mole fractions stood far above TE predictions. These measured CO_2 fractions were distributed on a trend line of slope 0.76 ($R^2 = 0.993$) passing through the origin of the graph. The comparison between TE and experimental data showed that combustion was not well represented by thermodynamics: the systematic absolute discrepancy was the result of reaction kinetic limitations. In Fig. 4-b, the measured CGE values are also plotted in a single O_2:C axis. Another clear trend was observed, as the CGE decreased linearly with increasing O_2:C ratio (function $y = 1.02 - 1.09x$, $R^2 = 0.940$). As a result, the impact of O_2:C ratio on both CO_2 emissions and CGE could precisely be assessed, which might provide precious indications for reactor design and control.

A dynamic assessment of the reactor thermal performance is provided in Fig. 5, showing the time evolution of the temperatures T_{pyro} (corresponding to solid phase for direct heating mode in Fig. 5-a; and emitter plate for indirect mode in Fig. 5-b), T_2 (reactor wall) and T_3 (cavity). When wood was injected, most of temperatures rose quickly because of combustion. The temperature measured by the pyrometer inside the cavity (direct heating mode, Fig. 5-a) always increased by
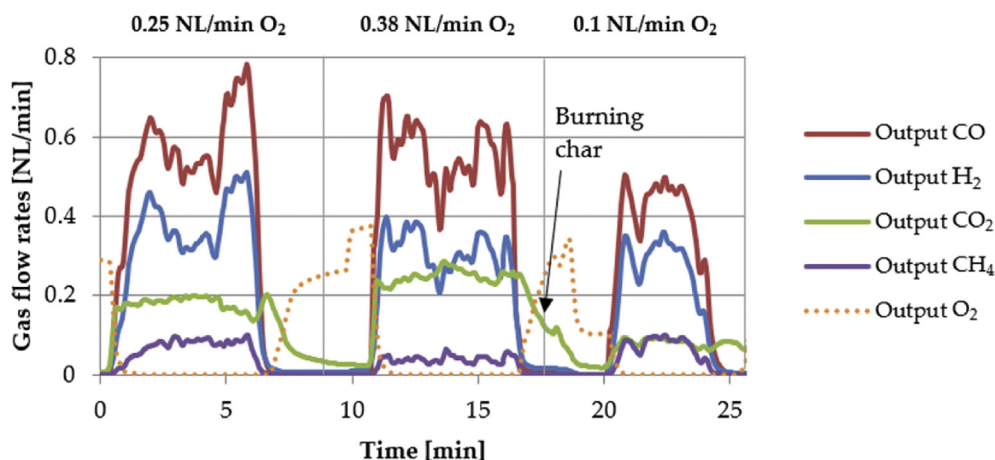
Fig. 2 − Flow rates of syngas components measured under different O_2 injection rates (run #2).
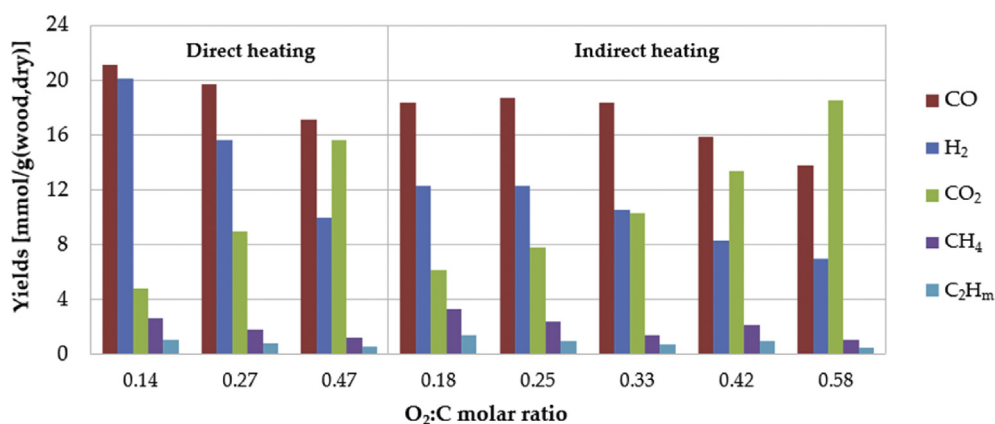

Fig. 3 − Yields of syngas components measured under increasing O_2:C molar ratios, in direct (run #1) and indirect (run #2) heating modes.

at least 100 °C with O_2, confirming that a hot flame appeared regardless of the quantity of oxygen injected. The T_3 measurement increased when the oxygen injection rate was 0.25 or 0.38 NL/min, whereas it slightly decreased at 0.1 NL/min. Thus, there exists a minimal amount of O_2 required to heat the reactor cavity properly. At 0.25 NL/min, T_3 rose by 60 °C in direct heating mode versus 30 °C in indirect heating mode. At 0.38 NL/min, it rose by 150 °C in direct heating mode versus 70 °C in indirect heating mode. Direct heating therefore appeared more advantageous regarding thermal performances. As for T_2, it increased significantly only when 0.38 NL/min of O_2 was injected (until +200 °C in direct heating mode and +50 °C in indirect heating mode), revealing that the quantity of O_2 necessary to efficiently heat the reactor walls was higher than 0.25 NL/min.

In summary, the more oxygen was added, the better the entire reactor was heated. It appeared that combustion primarily affected the temperature in the spout region, which highlights a local heating of the reactor. This heating mode (autothermal) thus differed from the solar heating mode (by radiation) which was mainly directed toward the particles and reactor walls.

Impact of the combination of oxidizing agents

The effect of oxidizing gas composition on output syngas yields and reactor efficiency was investigated. It was first unraveled via gasification tests performed with only steam or oxygen injection, and compared with a test featuring no oxidant injection at all (pyrolysis case). Hybrid gasification was then assessed by injecting both H_2O and O_2. Measurements were performed under a similar cavity temperature (~1240 °C) and in indirect heating mode. A summary of experimental conditions is reported in Table 3. The input flow rates of biomass (B), steam (S), and oxygen (O) are given, as well as the corresponding steam/biomass and equivalence ratios (ratios between proportions injected in the reactor and stoichiometric proportions of Equations (1) and (2), respectively). H_2O was always provided in slightly over-stoichiometric quantities. In contrast, oxygen was provided in highly under-stoichiometric quantities, as only 0.2 g/min of wood was intended to be burnt.

Experimental conditions are summed up in Fig. 6, and the lines of constant H_2:CO ratio and CGE calculated at TE are plotted in the (O_2:C; H_2O:C) plane. Because of the biomass
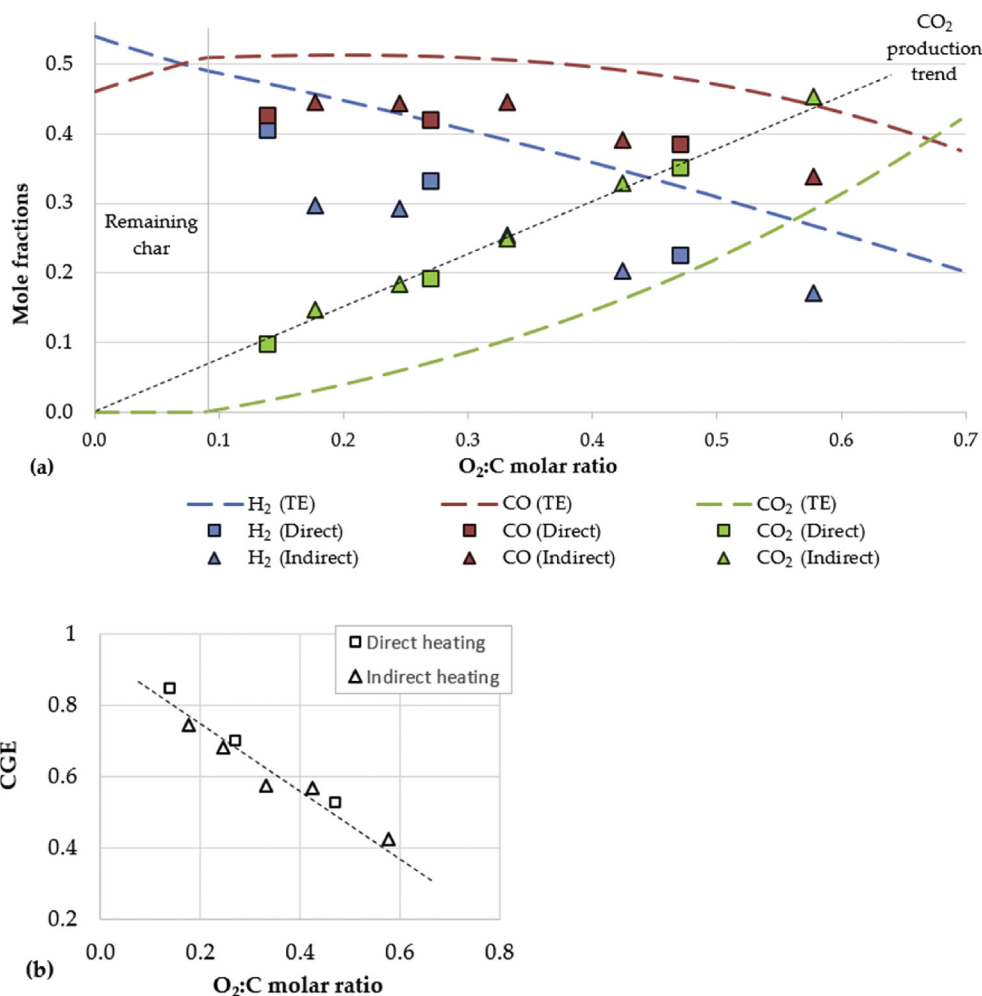
Fig. 4 − (a) Mole fractions of H_2, CO, and CO_2 measured under increasing O_2:C ratios, in direct (run #1, squares) and indirect (run #2, triangles) heating modes, compared with values calculated at TE (1200 °C, dashed lines). (b) CGE measured under increasing O_2:C ratios.

moisture content, the minimal H_2O:C ratio equals 0.134. The domain where char cannot be totally converted is found below the red line. It shows that either 0.14 g/min of steam or 0.9 NL/min of oxygen are necessary to gasify all the char at equilibrium. Then, addition of oxygen enables combustion, and addition of steam increases the H_2:CO ratio (via steam shifting). For example, TE predicts that the CGE undergoes an absolute decrease of 0.12 when O_2:C rises from 0.1 to 0.2, and that the H_2:CO ratio benefits from an absolute increase of 0.05 when H_2O:C rises from 0.3 to 0.4. Experimental series were performed to validate these theoretical trends.

Data used in this section stem from runs #2 (O_2-only case), #3 (pyrolysis case), #4 (hybrid case), and #8 (H_2O-only case). The corresponding syngas evolution curves are provided in Figs. S2, S3, S4, and 6-b. The O_2:C and H_2O:C molar ratios indicated in Fig. 6 are the ones calculated back after the experiments, as pointed out in the previous section. In the hybrid case, the actual values were always much higher than the expected ones because of rapidly decreasing wood injection rates: they reached 0.29 and 0.45 respectively (instead of 0.21 and 0.35 as calculated with the flow rates of Table 3).

A comprehensive comparison of the syngas yields and CGE obtained during the four experiments is provided in Fig. 7. Firstly, the syngas produced in the pyrolysis case had a similar composition than in the H_2O-only case, but with lower yields (divided by 2.0−2.8). This was explained by the insufficient (S/B)/(S/B)$_{st}$ ratio, equaling 0.43 in the pyrolysis case. In other words, only 43% of the char produced by pyrolysis could be gasified. This loss went with a decrease of the CGE by 53% (from 0.99 to 0.47) between H_2O-only and pyrolysis cases. Meanwhile, the syngas H_2:CO ratio equaled 1.25 in H_2O-only case versus only 1.15 in pyrolysis case, showing that excess steam might have facilitated water-gas shift (Equation (6)). Secondly, between pyrolysis and O_2-only cases, the CO yield increased whereas the H_2 yield remained the same. Both yields were expected to increase because of complete char conversion, but H_2 yield was not increased because it might have been partially consumed by combustion with O_2. The CGE was much higher (0.68 instead of 0.47 in the pyrolysis case), at the expense of increased CO_2 production yield (7.8 mmol/$g_{wood,dry}$ instead of 0.9 mmol/$g_{wood,dry}$ in the pyrolysis case). Finally, by comparing between O_2-only and hybrid
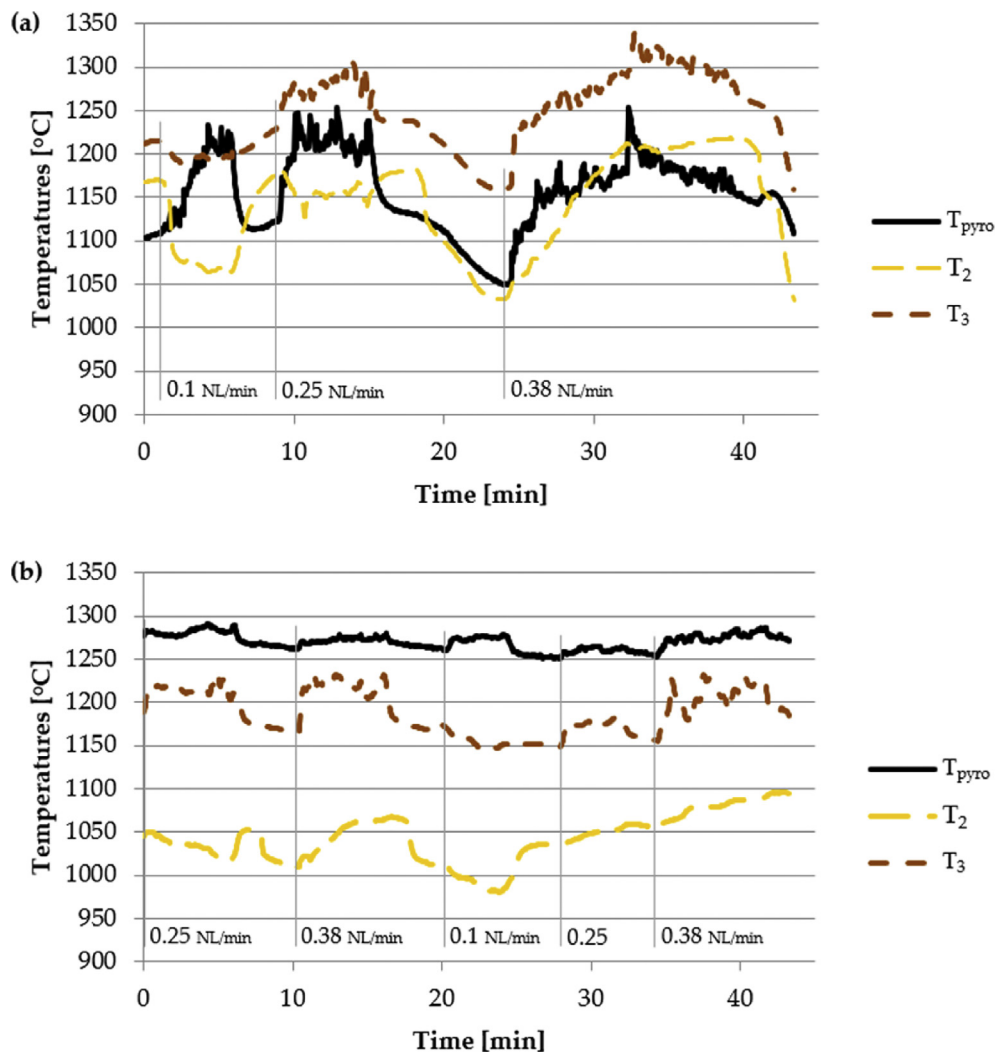
Fig. 5 — Temperatures evolution measured under different O_2 injection rates in (a) direct heating mode (run #1) and (b) indirect heating mode (run #2).

Table 3 — Gasification conditions for various mixtures of oxidizing agent.

Type of oxidant	Wood flow rate [g/min]	Steam flow rate [g/min]	Oxygen flow rate [NL/min]	(S/B)/(S/B)$_{st}$ ratio	Equivalence ratio (B/O)/(B/O)$_{st}$
∅	1.2	0	0	0.43	
H_2O	1.2	0.2	0	1.24	
O_2	1.2	0	0.25	0.43	4.31
$H_2O + O_2$	1.4	0.2	0.25	1.12	5.03

cases, the additional injection of water and biomass rose the H_2 yield from 12.3 to 14.8 mmol/$g_{wood,dry}$ and the CO_2 yield from 7.8 to 11.5 mmol/$g_{wood,dry}$. The CO yield did not differ significantly, resulting in a net increase of the H_2:CO ratio from 0.66 to 0.81.

These results provided insights into the impact of the various oxidizing agents. Tendencies found at TE (Fig. 6) were validated by experimental data (Fig. 7). As predicted, the highest H_2:CO ratio and CGE were measured in the H_2O-only case (1.25 and 0.99, respectively, while TE predicted values of 1.18 and 1.34). Experiments also confirmed that the H_2:CO

ratio during hybrid gasification was higher than during O_2-only gasification (0.81 versus 0.66) due to the addition of water. Lack of oxidizing agent (pyrolysis case) resulted in remaining char and lower gas yields while O_2 injection enabled some heat release by combustion associated with CO_2 production.

Impact of temperature on hybrid gasification under fixed solar power input

Runs #5 to #8 were performed to investigate the transition between allothermal and hybrid operation under a constant
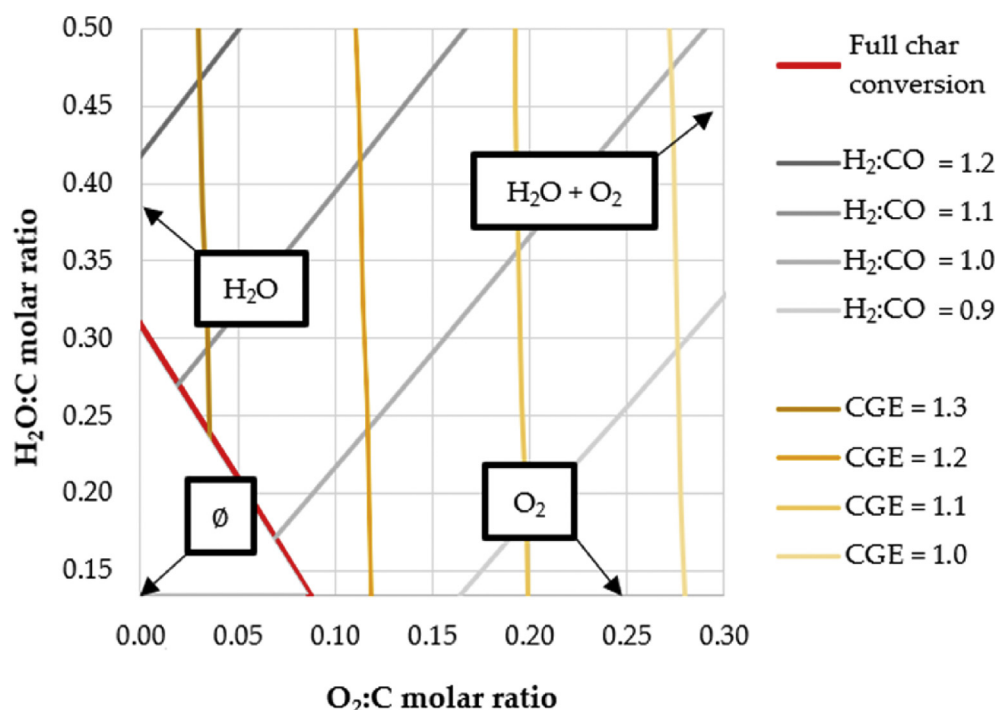
Fig. 6 — Lines of constant H_2:CO ratios and CGE, and limit of complete char conversion domain, computed at TE (1200 °C). Positions of the experimental runs conditions (pyrolysis, H_2O, O_2, $H_2O + O_2$) are indicated with arrows.
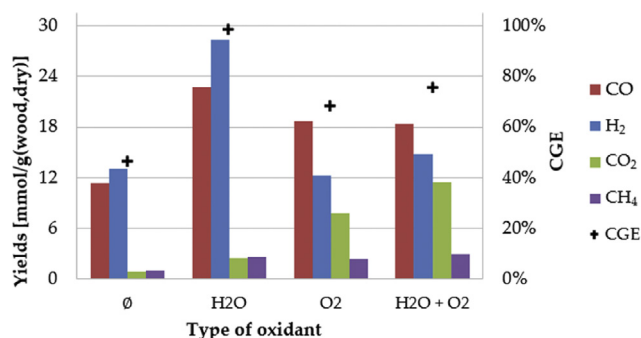

Fig. 7 — Yields of syngas components and CGE measured with different oxidizing gases (runs #3, #8, #2, and #4 from left to right).

solar power input. Runs #5 and #6 started near 1200 °C (T_3 measurement) and runs #7 and #8 started near 1300 °C. At first, a 1.2 g/min feeding rate of beech wood was gasified by a 0.2 g/min flow rate of steam (according to Equation (1)). After steady state was reached, an additional 0.2 g/min feeding rate of wood was provided and intended to be burnt by a 0.25 NL/min flow rate of oxygen (according to Equation (2)). Gasification was carried out in both direct (runs #5 and #7) and indirect (#6 and #8) heating modes. In Fig. 8, the flow rates of produced gases and the reactor temperatures obtained in indirect heating mode are shown (Fig. 8-a and Fig. 8-b for runs starting at 1200 °C and 1300 °C, respectively). The curves obtained in direct heating mode (runs #5 and #7) are provided in Supplementary Material (Fig. S5 and Fig. S6). In all cases, hybridization was characterized by a rise in the CO_2 flow rate, and by

the H_2 flow rate becoming lower than the CO one. The H_2 and CO production rates dropped with the depletion of the feedstock in the hopper, but the production of CO_2 continued for a few minutes as long as char remained in the cavity.

During allothermal gasification periods, T_2 and T_3 decreased because of the endothermic reaction occurring in the reactor. This cooling was faster when starting at 1200 °C: T_2 decreased by 105 °C in 5 min in run #6 versus 65 °C in 10 min in run #8. During hybrid operation, T_2 increased back at a rate of around 6.7 °C/min. T_3 increased continuously in run #8 (~4.7 °C/min), but in run #6 it quickly stagnated around 1200 °C. In both cases, the initial reactor temperatures were recovered when combustion occurred, and T_2 and T_3 values could even rise above their nominal values. Similar observations were done in direct heating mode (Fig. S5 and Fig. S6), with T_3 reaching back its initial value during hybrid operation. This confirmed the suitability of hybridization to overcome a potential loss of solar power.

The calculated syngas yields and CGE values are displayed in Fig. 9-a (1200 °C) and 9-b (1300 °C) along with TE predictions. Separate mass balances were performed for allothermal and hybrid time periods, in order to provide performance assessments. However, the uncertainty was higher than in Fig. 3 and Fig. 4-b, since the char accumulated in the cavity during allothermal gasification was not totally consumed before switching to hybrid gasification. Thus, the CGE values and the yields (especially CO_2) determined in allothermal operation might have been under-estimated by up to 10% as additional production of gases would be expected from gasification of this remaining char.

Experimental results showed a net decrease of H_2 yields between allothermal and hybrid operations (from 22.3 to
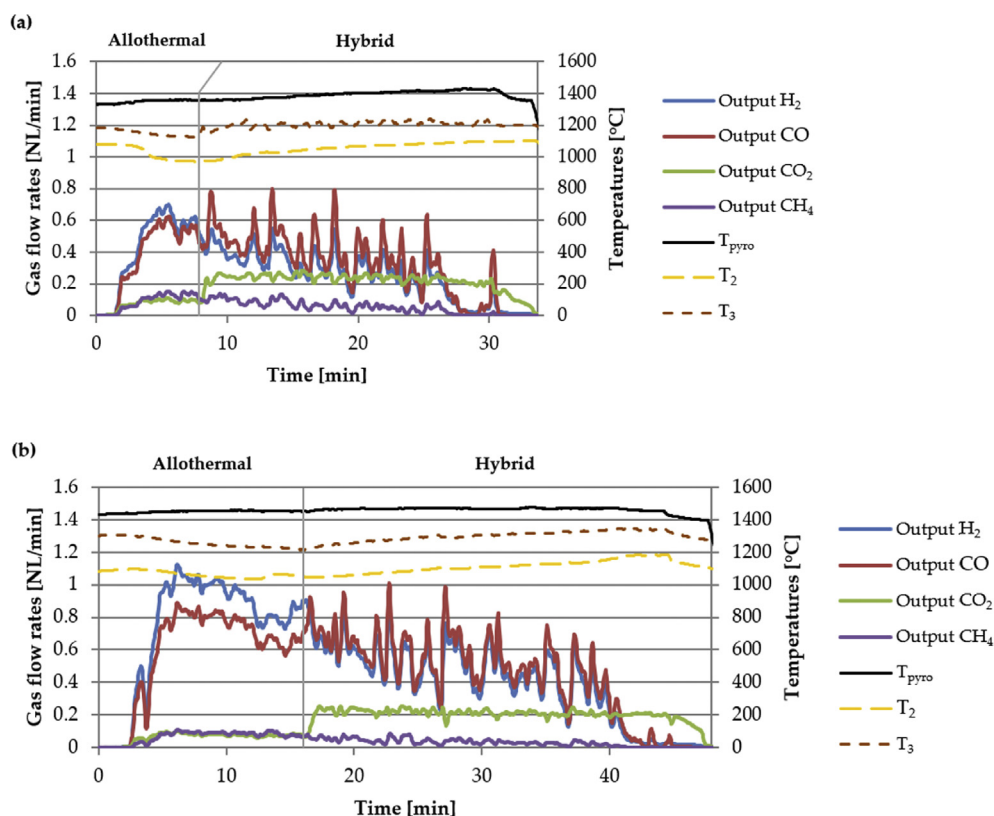
Fig. 8 — Flow rates of syngas components and temperatures measured during allothermal-hybrid runs, at a starting cavity temperature of (a) 1200 °C (run #6) and (b) 1300 °C (run #8).

13.4 mmol/$g_{wood,dry}$ at 1200 °C and from 28.4 to 19.7 mmol/$g_{wood,dry}$ at 1300 °C in indirect heating mode). The CO yield decreased as well at 1200 °C, but it almost did not change at 1300 °C. Meanwhile, hybridization caused the measured CO_2 yields to increase sharply (from 3.8 to 11.8 mmol/$g_{wood,dry}$ at 1200 °C and from 2.5 to 10.2 mmol/$g_{wood,dry}$ at 1300 °C in indirect heating mode). The CGE thus decreased between allothermal and hybrid gasification, with a higher loss observed at 1200 °C (from 1.01 to 0.70 in indirect heating mode) than at 1300 °C (from 0.99 to 0.78 in indirect heating mode). The same trends were observed in direct heating mode, though the performances obtained at 1200 °C were impaired by the emission of smoke (interruptions of gasification are visible in Fig. S5). Unlike experimental results, the TE predictions were not impacted by an increase of the nominal temperature. Thus, temperature impacted the reaction kinetics but not the system chemical equilibrium.

All these results allowed to precisely quantify the impact of temperature on the reactor performances in both allothermal and hybrid operating modes. In addition to provide insights into the dynamic transition between these two operation modes both in terms of temperature and species output, they showed that higher temperatures enabled to produce more H_2 and CO with lower amounts of CO_2 and CH_4, which was due to improved reaction kinetics. High temperatures also enabled to enhance the CGE during hybrid gasification.

Impact of heating mode during continuous hybrid operation

A first hint on the impact of heating mode was given in the previous section. Fig. 9 showed that a higher production of both H_2 and CO was usually obtained in direct heating mode, resulting in higher CGE values. During allothermal operation at 1300 °C, the CGE was estimated at 1.04 in direct heating mode versus 0.99 in indirect heating mode. During hybrid operation at 1300 °C, it was estimated at 0.88 in direct heating mode versus 0.78 in indirect heating mode. Boujjat et al. [46] indeed demonstrated that direct heating favored solar radiation absorption, with sunlight reaching directly the solid particles and the cavity walls. This experimental and numerical study showed that during allothermal gasification, the reacting bulk solid could locally reach much higher temperatures than the measured ones (they peaked at around 1500 °C). However, no comparison between direct and indirect heating modes was performed during hybrid gasification.

Continuous hybrid gasification was performed in runs #9 and #10 to precisely assess the gasification performances in direct and indirect heating modes, respectively. The T_3 temperature was initially set to 1200 °C thanks to the controlled opening of the shutter trapdoor. Water steam was then injected continuously in the reactor at a rate of 0.2 g/min, and oxygen and wood were provided at respective flow rates of 0.25 NL/min and 1.4 g/min. Steady hybrid operation was thus expected to settle during periods longer than in previous runs.
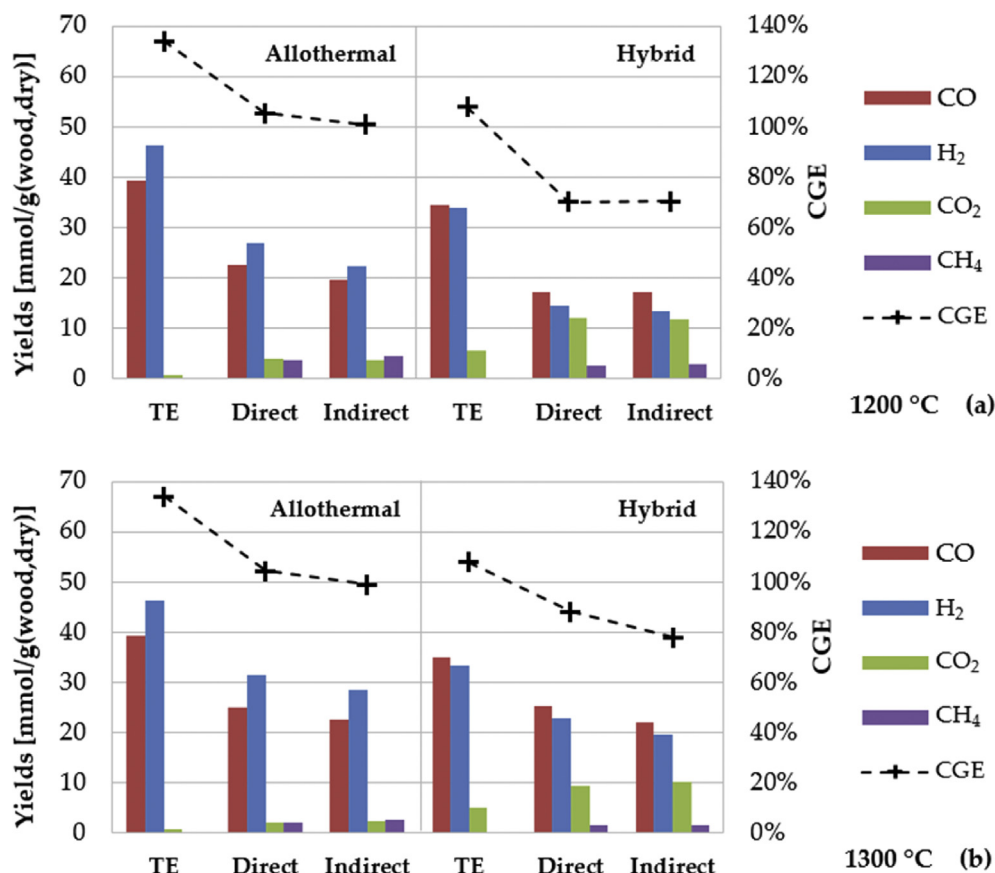
Fig. 9 — Yields of syngas components and CGE measured during allothermal-hybrid runs, and values calculated at TE, at a nominal cavity temperature of (a) 1200 °C (runs #5 and #6) and (b) 1300 °C (runs #7 and #8).

The output gas flow rates and the reactor temperatures of the two continuous runs are given in Fig. 10. In both direct (Fig. 10-a) and indirect (Fig. 10-b) heating modes, the volume flow rates of H_2 and CO reached values around 0.6 NL/min after 1 min of wood injection, and then oscillated with unequal amplitudes.

The fluctuations of syngas production rates were particularly noticeable in indirect heating mode (run #10). The CO_2 flow rate evolution, that used to remain steady in direct heating mode, had a much higher standard deviation in indirect heating mode (0.037 NL/min instead of 0.007 NL/min). Unsteady CO_2 production rate in indirect heating mode was also observed in runs #6 and #12, when compared with runs #5 and #11, respectively. Such oscillations might be caused by the emitter plate disturbing the gas flow between the cavity and the window, and leading to unexpected variations of the gas residence time.

Meanwhile, the reactor temperatures stabilized after 2 min of injection, and remained steady despite the variations of syngas production rates. T_3 rose by 105 °C in run #9 and by around 135 °C in run #10, and T_2 remained lower than or equal to its initial value. This tendency was in accordance with the observations in the section on the impact of oxygen injection flow-rate, confirming that hybrid operation was efficient to heat the reaction volume rather than the cavity walls. However, issues of pyrolytic smoke formation occurred. The injection of wood and oxygen was thus stopped during 3—5 min, once per run, to let the smoke dissipate. Because of these

interruptions, steady state operation could not be maintained more than 10 consecutive minutes. Furthermore, gasification could not be recovered after the interruption of run #10 (indirect heating, Fig. 10-b): the wall and emitter plate temperatures kept on decreasing despite the injection of reactants. This altered gasification regime resulted in an altered solar-to-fuel efficiency when compared to direct heating mode (16% instead of 24% for complete runs, as stated in Table 2). No such gap was found between direct and indirect heating among the other pairs of runs. Anyway, such high values denote that solar power is efficiently exploited during hybrid gasification.

Global experimental outcomes are summarized in Table 4, providing the syngas yields and reactor efficiencies calculated over the entire runs. Regarding the mass balance, 27.9 and 25.6 g of wood were injected in runs #9 and #10, respectively. In direct heating mode, 12.05 g of residue (solid particles along with unconverted water) were weighed in the outlet reactor components (tubing, bubbler and filter), leading to a mass balance closure of 96%. Regarding the CCE, it equaled 83.7% in direct heating mode and 86.2% in indirect heating mode. The CGE equaled ~82% in both heating modes. However, despite similar CGE values, direct heating mode offered higher H_2 and CO yields and lower CO_2, CH_4 and C_2H_m yields.

These continuous gasification runs confirmed that stable temperatures could be reached during hybrid gasification, with the cavity volume being heated while the walls remained at their initial temperature. The direct heating mode enabled a
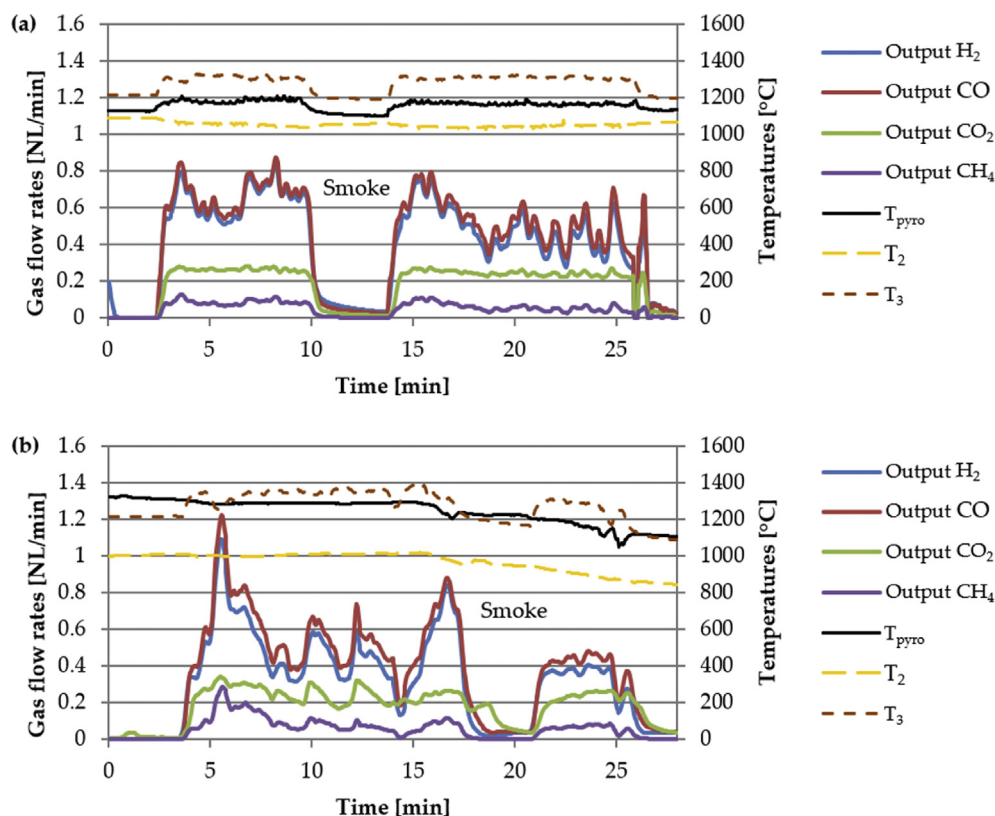
Fig. 10 — Flow rates of syngas components and temperatures measured during continuous hybrid runs, in (a) direct (run #9) and (b) indirect (run #10) heating modes.

Table 4 — Yields of syngas components, energy breakdown (lower heating values and solar energy absorbed by the reactor), and efficiencies measured during continuous hybrid runs (runs #9 and #10).

Run	Yields [mmol/g$_{wood, dry}$]					Energy breakdown [kJ]			Efficiencies		
	H_2	CO	CO_2	CH_4	C_2H_m	Biomass	Syngas	Solar Power	CCE	CGE	SFE
#9	19.17	20.59	8.78	2.49	1.11	426	351	1060	83.7%	82.4%	23.6%
#10	16.67	19.66	9.80	3.13	1.31	391	320	1656	86.2%	81.6%	15.6%

superior production of both H_2 and CO, even if the lower production of C_2H_m tended to bring the CGE down to the same value than in indirect heating mode. This confirmed that direct heating of the gasifier improved its performance, in addition to ensuring a better stability of the syngas production rate in the lab-scale reactor.

Hybrid gasification after a drop of solar power input

In this last section, the transition between allothermal and hybrid gasification was performed to compensate for a drop of solar power input and to demonstrate the feasibility of continuous operation with a variation of solar irradiation conditions. The T_3 temperature was first stabilized at ~1330 °C, and allothermal operation was started. After steady state was reached, the trapdoor was partially closed, making the solar power drop by 40% (from ~1200 W to ~700 W). After the trapdoor closure, oxygen and additional wood were injected. Fig. 11 shows the evolution of syngas production rates and reactor temperatures, in both direct (run #11, Fig. 11-

a) and indirect (run #12, Fig. 11-b) heating modes. In both cases, when the trapdoor was partially closed, all the temperatures decreased immediately due to the solar power reduction. When oxygen was added, temperatures evolved as follows:

- The temperature of the wall (T_2) kept on decreasing slowly despite combustion, reaching a value 200 °C lower than its initial value. Meanwhile, the temperature of the emitter plate (T_{pyro} in indirect heating mode, Fig. 11-b) decreased slowly until reaching 1400 °C;
- The temperature in the cavity (T_3) rose by 150 °C in less than 2 min, and then seemed to decrease slowly on the long term. The temperature of the bulk solid (T_{pyro} in direct heating mode, Fig. 11-a) followed the same variations.

The center of the cavity was thus maintained near its initial temperature ($T_3 \approx 1330$ °C) during the 10-min hybrid period, while the reactor walls tended to cool down because of a lower solar power input. As suggested previously,
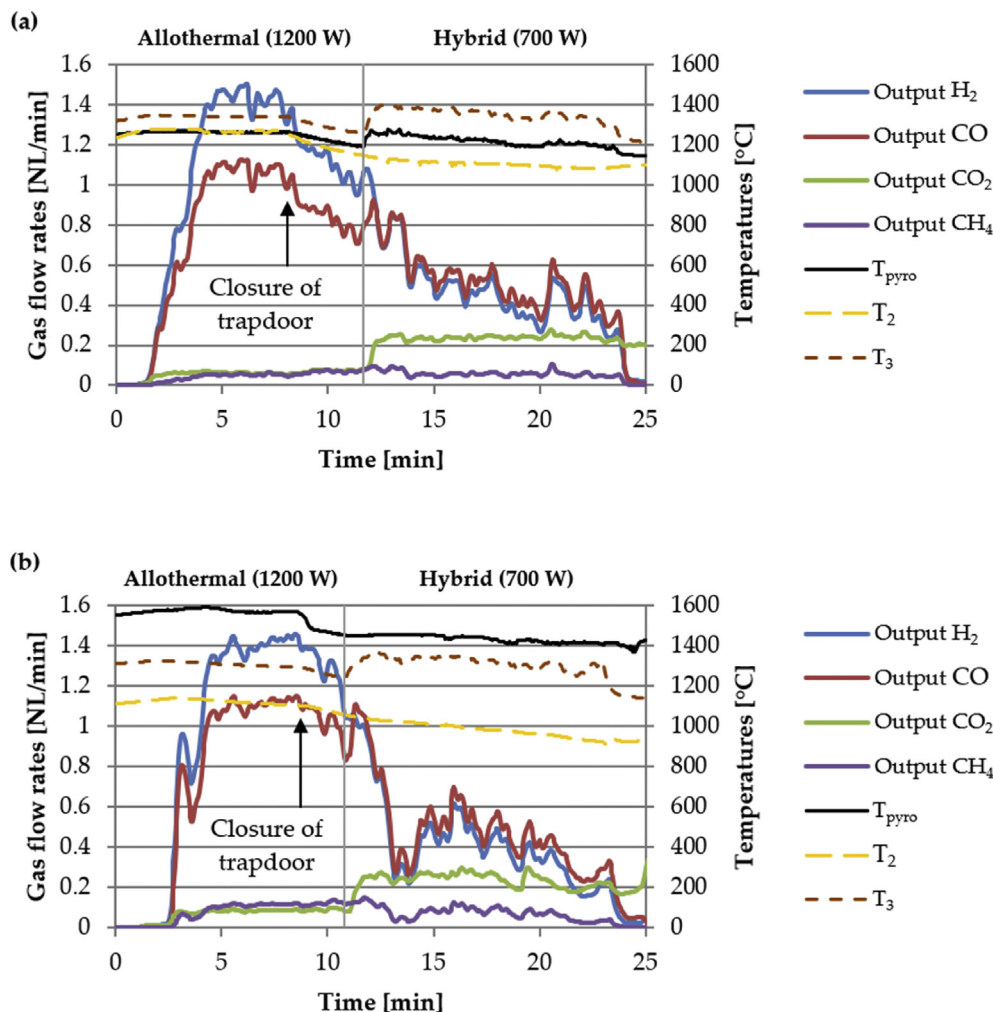
Fig. 11 — Flow rates of syngas components and temperatures measured during allothermal-hybrid runs featuring a 40% decrease of the solar power input, in (a) direct (run #11) and (b) indirect (run #12) heating modes.

combustion was suitable to heat the reaction volume very locally, which translated into T_3 being maintained despite a cut of 500 W of the incident solar power. In comparison, combustion of biomass feedstock by 0.25 NL/min of oxygen would release only 71 W, while combustion of carbon monoxide alone would release a threshold power of 104 W (versus 88 W for hydrogen combustion, based on standard enthalpies). Besides, the solar-to-fuel efficiency was calculated over the entire runs, and it equaled 27.4% and 28.3% in direct and indirect heating modes, respectively. These values were higher than those of the previous runs, confirming that solar power was suitably exploited despite the cooling of the cavity walls.

The syngas composition (Fig. 12) was evaluated and compared with runs #5 to #8. The performance of allothermal gasification was higher than in Fig. 9-b thanks to a higher starting temperature (1330 °C). The H_2 yields were increased to 36.0 and 31.6 mmol/$g_{wood,dry}$ (direct and indirect heating modes, respectively), the CO yields to 27.1 and 24.9 mmol/$g_{wood,dry}$, and the calculated CGE to 110.2% and 107.4%. Meanwhile, the CO_2 yields remained as low as 2 mmol/$g_{wood,dry}$. Regarding hybrid gasification, the syngas yields were rather comparable to those of Fig. 9-b. The calculated CGE reached respectively 0.89 and 0.92 during hybrid operation.

The drop of solar power input was therefore counterbalanced by a local heating of the cavity center. While the reaction volume was maintained to its initial temperature, the cavity walls cooled down because of the decreased solar power input, which delayed the establishment of a new
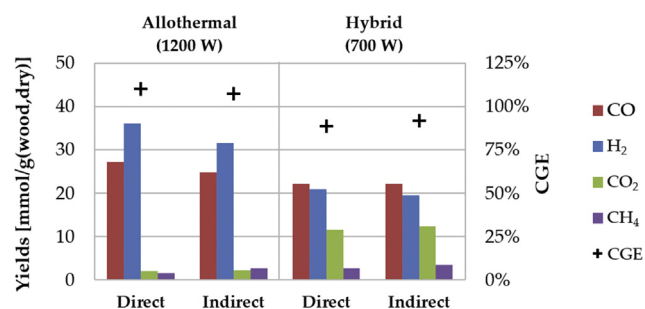

Fig. 12 — Yields of syngas components and CGE measured during allothermal-hybrid runs featuring a 40% decrease of the solar power input (runs #11 and #12).

steady state in the reactor. Even if the syngas quality was affected by hybridization, acceptable performance outputs were obtained, leading to an overall CGE of 100% in both runs #11 and #12. Thus, continuous operation under fluctuating solar irradiation conditions appeared feasible in this hybridized reactor.

Conclusion

The experimental study of a spouted-bed solar gasifier demonstrated that hybridization was effective to heat the gasifier cavity and compensate for drops of solar power input. Oxygen was injected during hybrid solar-autothermal operation to compensate solar radiation decrease by combustion, which created a local heating of the cavity volume in the spout region where combustion occurred. The following results and conclusions were achieved:

- Clear relationships were found between the inlet O_2:C ratio, and the CO_2 mole fraction and CGE. Experimental values differed from those predicted at TE, because of kinetic limitation.
- The addition of steam allowed to gasify the feedstock while rising the syngas H_2:CO ratio. Mixed injection of H_2O and O_2 would thus enable to heat the reactor while controlling the syngas composition, according to thermodynamic equilibrium. This was demonstrated during hybrid runs. The impact of hybridization on syngas production yields was quantified in both direct and indirect heating modes, at nominal temperatures of 1200 °C and 1300 °C.
- Higher reaction temperatures allowed to reach higher H_2 and CO yields and lower CO_2 yields, thanks to improved reaction kinetics.
- Direct heating was more beneficial than indirect heating, as it enhanced the H_2 and CO yields thanks to better heating of the particles. The stability of syngas production was also improved.
- Hybridization, performed after a 40% drop of the solar power input, was suitable to maintain the cavity temperature at around 1350 °C. An overall CGE of 100% was found over the entire runs, featuring 10 min of allothermal gasification followed by 10 min of hybrid gasification.

This study showed the possibility to dynamically control a solar-driven wood gasifier and also provided valuable information about thermal and chemical transient behaviors during change in operating mode between allothermal (solar) and hybrid gasification. It paves the way toward control strategies implementation, by giving orders of magnitude of hybrid operation performance outputs. In further studies, longer hybrid series will be performed with optimized mixtures of oxidants, to better control the performance outputs of hybrid gasification. A dynamic simulation tool will then be developed for controlling the gasification process stability during continuous hybrid operation despite solar resource variability, via the implementation of an accurate hybrid control strategy.

Declaration of competing interest

The authors declare that they have no known competing financial interests or personal relationships that could have appeared to influence the work reported in this paper.

Acknowledgements

Appendix A. Supplementary data

Supplementary data to this article can be found online at https://doi.org/10.1016/j.ijhydene.2021.09.008.

REFERENCES

[1] Gregg DW, Taylor RW, Campbell JH. Solar gasification of coal, activated carbon, coke and coal and biomass mixtures. Sol Energy 1980;25:353–64. https://doi.org/10.1016/0038-092X(80)90347-3.

[2] Boujjat H, Rodat S, Abanades S. Techno-economic assessment of solar-driven steam gasification of biomass for large-scale hydrogen production. Processes 2021;9:462. https://doi.org/10.3390/pr9030462.

[3] Abanades S, Rodat S, Boujjat H. Solar thermochemical green fuels production: a review of biomass pyro-gasification, solar reactor concepts and modelling methods. Energies 2021;14:1494. https://doi.org/10.3390/en14051494.

[4] Puig-Arnavat M, Tora EA, Bruno JC, Coronas A. State of the art on reactor designs for solar gasification of carbonaceous feedstock. Sol Energy 2013;97:67–84. https://doi.org/10.1016/j.solener.2013.08.001.

[5] Chuayboon S, Abanades S. An overview of solar decarbonization processes, reacting oxide materials, and thermochemical reactors for hydrogen and syngas production. Int J Hydrogen Energy 2020;45:25783–810. https://doi.org/10.1016/j.ijhydene.2020.04.098.

[6] Taylor RW, Berjoan R, Coutures JP. Solar gasification of carbonaceous materials. Sol Energy 1983;30:513–25. https://doi.org/10.1016/0038-092X(83)90063-4.

[7] Piatkowski N, Steinfeld A. Solar-driven coal gasification in a thermally irradiated packed-bed reactor. Energy Fuels 2008;22:2043–52. https://doi.org/10.1021/ef800027c.

[8] Flechsenhar M, Sasse C, Luft DS-D. Solar gasification of biomass using oil shale and coal as candidate materials. Energy 1995;20:803–10.

[9] Bellouard Q, Abanades S, Rodat S, Dupassieux N. Solar thermochemical gasification of wood biomass for syngas production in a high-temperature continuously-fed tubular reactor. Int J Hydrogen Energy 2017;42:13486–97. https://doi.org/10.1016/j.ijhydene.2016.08.196.

[10] Gokon N, Izawa T, Abe T, Kodama T. Steam gasification of coal cokes in an internally circulating fluidized bed of thermal storage material for solar thermochemical processes. Int J Hydrogen Energy 2014;39:11082–93. https://doi.org/10.1016/j.ijhydene.2014.05.124.

[11] Zgraggen A, Haueter P, Trommer D, Romero M, Dejesus J, Steinfeld A. Hydrogen production by steam-gasification of petroleum coke using concentrated solar power—II reactor design, testing, and modeling. Int J Hydrogen Energy 2006;31:797–811. https://doi.org/10.1016/j.ijhydene.2005.06.011.

[12] Matsunami J, Yoshida S, Oku Y, Yokota O, Tamaura Y, Kitamura M. Coal gasification by CO2 gas bubbling in molten salt for solar/fossil energy hybridization. Sol Energy 2000;68:257–61. https://doi.org/10.1016/S0038-092X(99)00074-2.

[13] Bruckner AP. Continuous duty solar coal gasification system using molten slag and direct-contact heat exchange. Sol Energy 1985;34:239–47. https://doi.org/10.1016/0038-092X(85)90061-1.

[14] Milanese M, Colangelo G, Iacobazzi F, de Risi A. Modeling of double-loop fluidized bed solar reactor for efficient thermochemical fuel production. Sol Energy Mater Sol Cell 2017;160:174–81. https://doi.org/10.1016/j.solmat.2016.10.028.

[15] Suárez-Almeida M, Gómez-Barea A, Ghoniem AF, Pfeifer C. Solar gasification of biomass in a dual fluidized bed. Chem Eng J 2021;406:126665. https://doi.org/10.1016/j.cej.2020.126665.

[16] Gómez-Barea A, Suárez-Almeida M, Ghoniem A. Analysis of fluidized bed gasification of biomass assisted by solar-heated particles. Biomass Convers Biorefin 2021;11:143–58. https://doi.org/10.1007/s13399-020-00865-0.

[17] Guo P, van Eyk PJ, Saw WL, Ashman PJ, Nathan GJ, Stechel EB. Performance assessment of Fischer–Tropsch liquid fuels production by solar hybridized dual fluidized bed gasification of lignite. Energy Fuels 2015;29:2738–51. https://doi.org/10.1021/acs.energyfuels.5b00007.

[18] Müller F, Poživil P, van Eyk PJ, Villarrazo A, Haueter P, Wieckert C, Nathan GJ, Steinfeld A. A pressurized high-flux solar reactor for the efficient thermochemical gasification of carbonaceous feedstock. Fuel 2017;193:432–43. https://doi.org/10.1016/j.fuel.2016.12.036.

[19] Dai S, Chang Z, Chang C, Akhatov JS, Li X. Numerical study on the directly-irradiated vortex reactor for solar CO2 coal gasification. Sol Energy 2019;188:573–85. https://doi.org/10.1016/j.solener.2019.06.035.

[20] Bellouard Q, Abanades S, Rodat S. Biomass gasification in an innovative spouted-bed solar reactor: experimental proof of concept and parametric study. Energy Fuels 2017;31:10933–45. https://doi.org/10.1021/acs.energyfuels.7b01839.

[21] Bellouard Q, Rodat S, Abanades S, Ravel S, Frayssines P-É. Design, simulation and experimental study of a directly-irradiated solar chemical reactor for hydrogen and syngas production from continuous solar-driven wood biomass gasification. Int J Hydrogen Energy 2019;44:19193–205. https://doi.org/10.1016/j.ijhydene.2018.04.147.

[22] Chuayboon S, Abanades S, Rodat S. Experimental analysis of continuous steam gasification of wood biomass for syngas production in a high-temperature particle-fed solar reactor. Chem Eng Process 2018;125:253–65. https://doi.org/10.1016/j.cep.2018.02.004.

[23] Matsunami J, Yoshida S, Oku Y, Yokota O, Tamaura Y, Kitamura M. Coal gasification by CO2 gas bubbling in molten salt for solar/fossil energy hybridization. Sol Energy 2000;68:257–61. https://doi.org/10.1016/S0038-092X(99)00074-2.

[24] Hathaway BJ, Davidson JH. Demonstration of a prototype molten salt solar gasification reactor. Sol Energy 2017;142:224–30. https://doi.org/10.1016/j.solener.2016.12.032.

[25] Boujjat H, Rodat S, Abanades S. Solar-hybrid thermochemical gasification of wood particles and solid recovered fuel in a continuously-fed prototype reactor. Energies 2020;13:5217. https://doi.org/10.3390/en13195217.

[26] Boujjat H, Rodat S, Chuayboon S, Abanades S. Experimental and numerical study of a directly irradiated hybrid solar/combustion spouted bed reactor for continuous steam gasification of biomass. Energy 2019;189:116118. https://doi.org/10.1016/j.energy.2019.116118.

[27] Mayers MA. The rate of oxidation of graphite by steam. J Am Chem Soc 1934;56:1879–81. https://doi.org/10.1021/ja01324a015.

[28] Thomas JM. Reactivity of carbon: some current problems and trends. Carbon 1970;8:413–21. https://doi.org/10.1016/0008-6223(70)90001-1.

[29] Diblasi C. Modeling chemical and physical processes of wood and biomass pyrolysis. Prog Energy Combust Sci 2008;34:47–90. https://doi.org/10.1016/j.pecs.2006.12.001.

[30] Cai J, Wu W, Liu R. An overview of distributed activation energy model and its application in the pyrolysis of lignocellulosic biomass. Renew Sustain Energy Rev 2014;36:236–46. https://doi.org/10.1016/j.rser.2014.04.052.

[31] Vakalis S, Patuzzi F, Baratieri M. Thermodynamic modeling of small scale biomass gasifiers: development and assessment of the "multi-box" approach. Bioresour Technol 2016;206:173–9. https://doi.org/10.1016/j.biortech.2016.01.060.

[32] Cortazar M, Alvarez J, Lopez G, Amutio M, Santamaria L, Bilbao J, Olazar M. Role of temperature on gasification performance and tar composition in a fountain enhanced conical spouted bed reactor. Energy Convers Manag 2018;171:1589–97. https://doi.org/10.1016/j.enconman.2018.06.071.

[33] Chuayboon S, Abanades S, Rodat S. Comprehensive performance assessment of a continuous solar-driven biomass gasifier. Fuel Process Technol 2018;182:1–14. https://doi.org/10.1016/j.fuproc.2018.10.016.

[34] Chuayboon S, Abanades S, Rodat S. Insights into the influence of biomass feedstock type, particle size and feeding rate on thermochemical performances of a continuous solar gasification reactor. Renew Energy 2019;130:360–70. https://doi.org/10.1016/j.renene.2018.06.065.

[35] Boujjat H, Rodat S, Chuayboon S, Abanades S. Experimental and CFD investigation of inert bed materials effects in a high-temperature conical cavity-type reactor for continuous solar-driven steam gasification of biomass. Chem Eng Sci 2020;228:115970. https://doi.org/10.1016/j.ces.2020.115970.

[36] Yoon HC, Cooper T, Steinfeld A. Non-catalytic autothermal gasification of woody biomass. Int J Hydrogen Energy 2011;36:7852–60. https://doi.org/10.1016/j.ijhydene.2011.01.138.

[37] Li X, Shen Y, Kan X, Hardiman TK, Dai Y, Wang C-H. Thermodynamic assessment of a solar/autothermal hybrid gasification CCHP system with an indirectly radiative reactor. Energy 2018;142:201–14. https://doi.org/10.1016/j.energy.2017.09.149.

[38] Petrasch J, Osch P, Steinfeld A. Dynamics and control of solar thermochemical reactors. Chem Eng J 2009;145:362–70. https://doi.org/10.1016/j.cej.2008.07.051.

[39] Saade E, Clough DE, Weimer AW. Model predictive control of a solar-thermal reactor. Sol Energy 2014;102:31–44. https://doi.org/10.1016/j.solener.2013.12.029.

[40] Muroyama A, Shinn T, Fales R, Loutzenhiser PG. Modeling of a dynamically-controlled hybrid solar/autothermal steam

gasification reactor. Energy Fuels 2014;28:6520–30. https://doi.org/10.1021/ef501535r.

[41] Boujjat H, Yuki Junior GM, Rodat S, Abanades S. Dynamic simulation and control of solar biomass gasification for hydrogen-rich syngas production during allothermal and hybrid solar/autothermal operation. Int J Hydrogen Energy 2020;45:25827–37. https://doi.org/10.1016/j.ijhydene.2020.01.072.

[42] Muroyama AP, Guscetti I, Schieber GL, Haussener S, Loutzenhiser PG. Design and demonstration of a prototype 1.5 kWth hybrid solar/autothermal steam gasifier. Fuel 2018;211:331–40. https://doi.org/10.1016/j.fuel.2017.09.059.

[43] Hathaway BJ, Davidson JH. Autothermal hybridization and controlled production of hydrogen-rich syngas in a molten salt solar gasifier. Int J Hydrogen Energy 2021:S0360319921005322. https://doi.org/10.1016/j.ijhydene.2021.02.048.

[44] Boujjat H, Rodat S, Abanades S, Perret C. Simulation of biomass gasification in a novel high-temperature directly irradiated hybrid solar/combustion reactor. In: Casablanca, Morocco; 2019. p. 180005. https://doi.org/10.1063/1.5117685.

[45] Goodwin DG, Moffat HK, Speth RL. Cantera: an object-oriented software toolkit for chemical kinetics, thermodynamics, and transport processes. Version 2.2.1. Zenodo 2016. https://doi.org/10.5281/zenodo.45206.

[46] Boujjat H, Rodat S, Chuayboon S, Abanades S. Numerical simulation of reactive gas-particle flow in a solar jet spouted bed reactor for continuous biomass gasification. Int J Heat Mass Tran 2019;144:118572. https://doi.org/10.1016/j.ijheatmasstransfer.2019.118572.